Imaging backscattering in graphene quantum point contacts

A. Mreńca-Kolasińska* and B. Szafran

AGH University of Science and Technology, Faculty of Physics and Applied Computer Science, aleja Mickiewicza 30, 30-059 Kraków, Poland

(Received 28 April 2017; published 24 October 2017)

We study graphene quantum point contacts (QPCs) and imaging of the backscattering of the Fermi level wave function by potential introduced by a scanning probe. We consider both etched single-layer QPCs as well as the ones formed by bilayer patches deposited on the sides of the monolayer conducting channel. An atomistic tight-binding method is developed to effectively simulate an infinite graphene plane outside the QPCs using a computational box of a finite size. We demonstrate that in spite of the Klein phenomenon interference effects due to the backscattering at a circular $n-p$ junction induced by the probe potential are visible in spatial conductance maps.

DOI: 10.1103/PhysRevB.96.165310

I. INTRODUCTION

Quantum point contacts [1,2] (QPCs) are elementary building blocks of quantum transport devices for carrier injection and readout with control over the quantized conductance. Transport phenomena for the current injected through QPCs are studied with the spatial resolution using scanning gate microscopy (SGM) [3], a technique in which the charged tip of the atomic force microscope perturbs the potential within the system with the two-dimensional electron gas (2DEG), induces backscattering, and alters the conductance. SGM was used for graphene-based systems, the QPCs [4] including states localized within the constriction [5–7], quantum Hall conditions [8–10], and magnetic focused trajectories [11,12]. Theoretical studies for magnetic focusing [13] and imaging snake states [14] were performed.

SGM for QPCs defined within the two-dimensional electron gas for heterostructures based on III-V semiconductors resolves interference of the incident and backscattered [15–19] wave functions. In graphene, a strong tip potential induces formation of a local $n-p$ junction [20] instead of depletion of the electron gas as in III-V semiconductors. The $n-p$ junctions in graphene are transparent for normally incident Fermi level electrons due to the Klein tunneling [21–24]. Nevertheless, we show that the backscattering induced by the $n-p$ junction formed by the tip induces a clear interference in SGM maps with a period of half the Fermi wavelength.

In semiconductor heterostructures with a 2DEG, QPCs can be defined by lateral gates, which deplete the 2DEG and thus change the constriction width and narrow the conduction channel for Fermi level electrons [2]. In graphene the channel constriction by external gates is ineffective due to Klein tunneling [25]. Etched QPCs were studied instead by both experiment [26–29] and theory [30–32]. In bilayer graphene [33–35] it is possible to induce a band gap by applying a bias between the layers [36–38]. QPCs on graphene with bilayer inclusions have been produced [10], but conductance quantization in these systems has not been theoretically investigated so far. For a demonstration that the present results are independent of the QPC type we consider both etched [Fig. 1(a)] and bilayer patched QPCs [Fig. 1(b)]. The latter turn out to be less susceptible to perturbation by defects within the QPCs.

*Corresponding author: alina.mrenca@fis.agh.edu.pl

In order to discuss the effects of the sample imperfections we consider defects both at the edge and within the bulk of the sample. For the edge defects we consider singly connected carbon atoms [39] protruding from the zigzag segments of the constriction edge that produce resonant scattering that destabilizes the conductance plateaux. For the bulk imperfections we consider local potential perturbation introduced by fluorine adatoms deposited on the surface [40].

II. THEORY

We use the atomistic tight-binding Hamiltonian spanned by p_z orbitals,

$$H = \sum_{\langle i,j\rangle}(t_{ij}c_i^\dagger c_j + \text{H.c.}) + \sum_i V(\mathbf{r}_i)c_i^\dagger c_i, \tag{1}$$

where $V(\mathbf{r}_i)$ is the external potential at the ith site at position $\mathbf{r}_i$ and in the first term we sum over the nearest neighbors. We use the tight-binding parametrization of Ref. [41], with $t_{ij} = -3.12$ eV for the nearest neighbors within the same layer. For the bilayer, we take $t_{ij} = -0.377$ eV for the A-B dimers, $t_{ij} = -0.29$ eV for skew interlayer hoppings [41] between atoms of the same sublattice (A-A or B-B type), and $t_{ij} = 0.12$ eV for skew interlayer hopping between atoms of different sublattices. The potential energy in the lower layer is taken as the reference level $V_b' = 0$, and the value of the upper layer V_b is tuned by the electric field perpendicular to the layer. The interlayer distance is 3.32 Å.

In order to account for the effects of the lattice imperfections far from the edges of the sample we consider separate fluorine adatoms with the tight-binding parametrization of the hopping parameters taken from Ref. [40] in the dilute fluorination limit. Accordingly [40], for the hopping between the fluorine and the carbon atoms we take $T = 5.5$ eV, and the on-site energy on the fluorine ion is $\varepsilon_F = -2.2$ eV.

For simulation of the SGM, we assume an effective potential of the tip with a Lorentzian form [42],

$$V(x,y) = \frac{V_t}{1 + [(x-x_t)^2 + (y-y_t)^2]/d^2}, \tag{2}$$

where x_t, y_t are the tip coordinates, d is the effective width of the tip potential, and V_t is its maximal value ($V_t = 1.25$ eV unless stated otherwise).

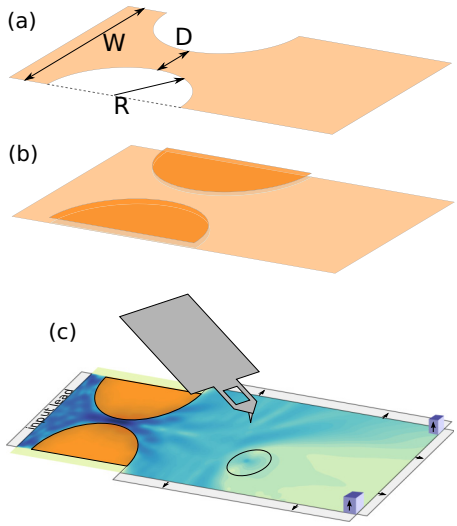

FIG. 1. QPCs (a) etched out of graphene and (b) built of patches of bilayer graphene. (c) Schematic drawing of the simulated scanning gate microscopy. The circle indicates the $n-p$ junction for the tip potential equal to the $V = E_F$. The light gray lines with the arrows indicate the open BCs introduced as leads. The electric blue blocks with the vertical arrows mark the additional leads used as a sink of currents to suppress backscattering by the corners.

We consider the energy range near the Dirac point. For evaluation of the transmission probability, we use the wave-function-matching (WFM) technique as described in Ref. [43]. The transmission probability from the input lead to mode m in the output lead is

$$T^m = \sum_n |t^{mn}|^2, \tag{3}$$

where t^{mn} is the probability amplitude for the transmission from the mode n in the input lead to mode m in the output lead. We evaluate the conductance as $G = G_0 \sum_m T^m$, with $G_0 = 2e^2/h$:

$$G = G_0 \sum_{m,n} |t^{mn}|^2. \tag{4}$$

We consider an armchair nanoribbon of width $W = 62$ nm, 509 atoms wide. The QPC is formed either by etched-out semicircles with radii $R = 28$ nm producing a QPC [Fig. 1(a)] or by bilayer patches of the same form [Fig. 1(b)]. The QPC is $D = 6$ nm wide at the narrowest point. We consider QPC edges with a number of singly connected atoms, similar to the ones present in the Klein edge [39,44] [Fig. 2(c)], as well as "clean" edges with the singly connected atoms removed [Fig. 2(d)]. For the SGM modeling, open boundary conditions (BCs) at the horizontal edges on the output QPC side are applied. We add to the right of the QPC, i.e., the output side, two leads that are semi-infinite in the y direction and extend all along the upper and lower edges of the nanoribbon [Fig. 3(c)]. The extra leads are introduced to simulate an infinite graphene sheet to eliminate the effects of the backscattering from the nanoribbon edges and the subband quantization that produces a set of subband-dependent Fermi wavelengths instead of a single one. Upon attachment of the leads, the corners of the computational box, between the right lead and the top or bottom leads [Fig. 1(c)], still act as scattering centers and produce an artificial interference.

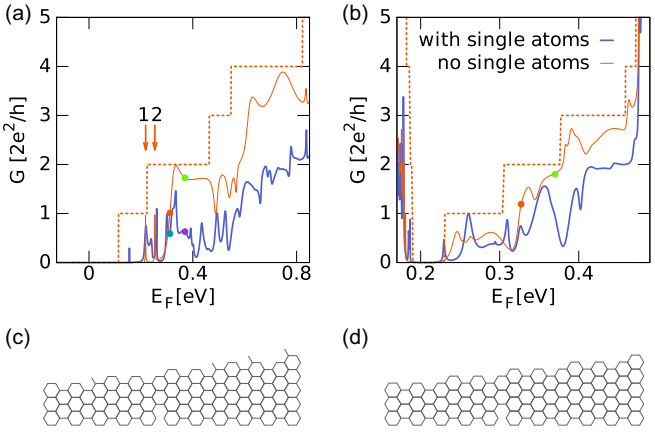

FIG. 2. The conductance of QPCs defined in an armchair nanoribbon with a width of 509 atoms across the ribbon by (a) etching and (b) bilayer patches. The dots mark the work points for the conductance mapping (see the text). The section of the etched QPC edge (c) with or (d) without single atoms.

To eliminate the scattering by the corners, which influences the SGM maps, we added in the top right and bottom right corners two leads that are semi-infinite in the z direction (Fig. 3) that absorb the current that has not entered the in-plane leads. The additional vertical leads are attached to the corners of the computational box as the sinks of the current. As the present approach is based on the atomistic tight-binding procedure, we had to choose an atomic structure form of the leads.

III. RESULTS

A. Conductance of the QPC constrictions

In Figs. 2(a) and 2(b) the transmission probability as a function of the Fermi energy is presented. A transport energy gap due to the constriction is present near the Dirac point. For QPCs with singly connected atoms at the etched edge [blue line in Fig. 2(a)], the conductance exhibits a number of sharp peaks.

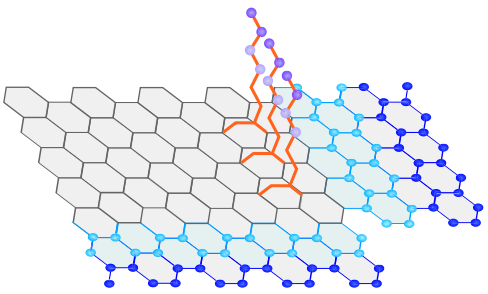

FIG. 3. The atomic structure of the corner of the computational box; the blue atoms indicate the area where the horizontal leads are attached. The horizontal leads preserve the crystal structure of graphene. The atoms marked in light blue belong to the elementary cell of the lead, and the dark blue atoms form the duplicate of the elementary cell that ensures periodicity of the leads. The vertical leads are marked with the orange lines. The hopping elements are taken to be equal to the nearest-neighbor hopping within graphene.

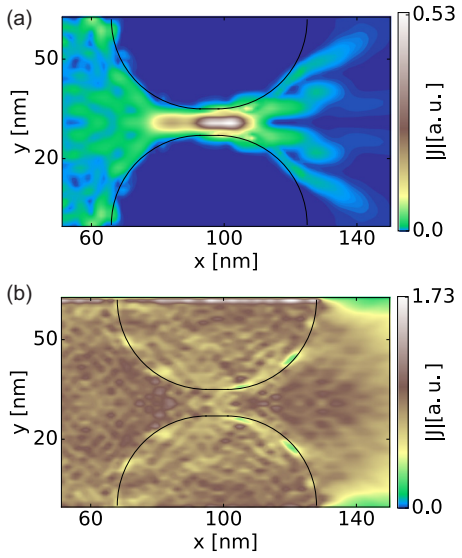

FIG. 4. The current densities in the QPC formed by biased bilayer patches at $E_F = 0.327$ eV (a), within the energy gap of bilayer patches that is (0.19,0.64) eV. In (b) $E_F = 0.764$ eV exceeds the bias and current flows across entire ribbon.

No well-developed plateaus are observed, and the conductance is much lower than the one for a uniform ribbon of the width of the narrowest part of the QPC (dashed line). This is caused by strong backscattering by the atomic-scale roughness of the etched QPC induced by the singly connected atoms. Upon their removal [see Figs. 2(c) and 2(d)], the conductance [the orange line in Fig. 2(a)] becomes a smooth function of the energy and approaches the maximal conductance for the QPC width.

For the bilayer patches we assume that the potential on the lower graphene layer is $V = 0$ and is V_b on the upper layer ($V_b = 0.64$ eV unless stated otherwise). For that bias within the finite-size bilayer patches a band gap is formed in the range of (0.19,0.64) eV. For the Fermi energy E_F of the leads within the gap opened by the interlayer bias in the constriction, the current does not penetrate the patches [Fig. 4(a)]. For E_F beyond the forbidden range the current flows across the patches [Fig. 4(b)]. Like for the etched QPCs, the geometry of the QPCs is specified once the sample is produced; however, the bilayer patched systems can be controlled via the electric field, which allows us to turn on and off the quantizing properties or alter the number of conducting modes in the QPCs.

The conductance of the patched QPCs is presented in Fig. 2(b) as a function of E_F. The dashed line shows the conductance of a uniform nanoribbon with two rectangular bilayer patches along the entire ribbon with a width matching the conditions of the narrowest point of the QPC constriction. The conductance of the QPCs with patches that contain a Klein edge and those without it is in both cases smooth; however, there is the ubiquitous backscattering that makes the conductance lower than that of the uniform ribbon with the same structure as the narrowest part of the QPC. With the singly connected atoms the $G(E_F)$ dependence is smoother in the patched QPC [Fig. 2(b)] than in the etched one [Fig. 2(a)] since even for the atoms of the upper layer that have only one neighbor in plane, there is a nonzero hopping to the atoms in the lower layer.

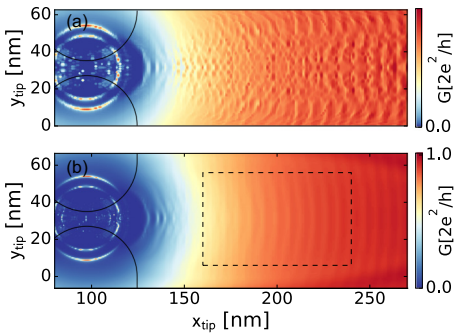

FIG. 5. The conductance of an etched QPC without the singly connected atoms for $E_F = 0.312$ eV [orange dot in Fig. 2(a)] as a function of the SGM tip position for (a) a 509-atom-wide nanoribbon on the right QPC side (closed BCs at the vertical edges) and (b) an infinite graphene half plane simulated with open BCs.

B. Simulation of the scanning gate microscopy

For $E_F < V_t = 1.25$ eV the tip introduces an $n-p$ junction. For QPCs without the singly connected atoms we choose the work point for the scanning maps at the conductance step ($G \approx G_0$) and at the plateau $G \approx 2G_0$. For the etched QPC the plateau and the step are taken at $E_F = 0.312$ eV [$G = 1.01G_0$; see the orange point in Fig. 2(a)] and $E_F = 0.37$ eV at the etched nanoribbon [$G = 1.73G_0$; see the green point in Fig. 2(a)], respectively. For the patched QPC we take $E_F = 0.37$ meV for the plateau [$G = 1.8G_0$; the green point in Fig. 2(b)] and $E_F = 0.327$ eV for the step [$G = 1.19G_0$; the orange point in Fig. 2(b)].

For the QPC conductance, in the absence of the tip, the open BCs at the output side of the QPC play no significant role. The conductance is nearly the same with rigid and open BCs for the vertical edges of the ribbon. This fact results from a negligible scattering by the horizontal edges that could reverse the current back through the QPC to the input lead. However, the open conditions are crucial for the conductance mapping.

Let us first consider conductance maps for closed BCs at the upper and lower edges of the ribbon, which are then the actual ends of the sample.

Figure 5(a) shows the conductance map for the etched QPC with the clean edge. The contour of the bilayer patch is marked by black solid lines. The two halos centered in the middle of the QPC correspond to the tip-induced activation of the two resonances marked by orange arrows in Fig. 2(a). Away from constriction in Fig. 5(a) the conductance fluctuates in an irregular way due to a large number of transversal modes with different k_F. The nanoribbon of the considered width has 19 modes at $E_F = 0.312$ eV and 22 modes at $E_F = 0.37$ eV. The image contains the signal of the superposition of waves with many different Fermi wavelengths with the intersubband scattering.

The maps become simpler once open BCs are applied to the right (output) side of the QPC to simulate an infinite graphene half plane. In the conductance maps for the etched QPC with open BCs [Fig. 5(b)] the QPC-centered halos remain the same

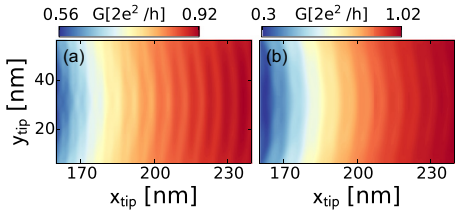

FIG. 6. Map of conductance within the region marked by the dashed rectangle in Fig. 5(a) for (a) etched and (b) patched QPCs. In both cases a clean QPC (patch) edge was taken, and a work point with large dG/dE_F was assumed, with (a) $E_F = 0.312$ eV and (b) $E_F = 0.327$ eV; see the orange dots in Fig. 2(a) and 2(b), respectively.

as for the closed BCs [Fig. 5(a)]. The difference occurs to the right of the QPC, where the simulated flake is infinite. Far from the QPC periodic oscillations of conductance are present. Figure 6 shows the zoom at the region [dashed line in Fig. 5(b)] for the etched [Fig. 6(a)] and patched [Fig. 6(b)] QPCs. In both scans the oscillations differ by an offset and not by the oscillation period.

C. QPC work point vs the conductance maps

The contrast of the conductance maps for fixed parameters of the tip potential depends on the Fermi energy. The contrast grows with the absolute value of the $\partial G/\partial E_F$ derivative. Figures 7 and 8 present the conductance maps for open boundary conditions with the work points marked by the orange and light green dots on the conductance vs the Fermi energy plot in Figs. 2(a) and 2(b), respectively. The maximal conductance value on the maps of Figs. 7 and 8 is given by the G values marked by the points on Figs. 2(a) and 2(b). The variation of the map increases with the $G(E_F)$ slope. The oscillation period in Figs. 7 and 8 is equal to half the Fermi wavelength.

D. Conductance maps and edge scatterers within the constriction

The singly connected atoms within the constrictions [Figs. 2(c) and 2(d)] are a strong source of scattering for electron waves that cross the QPCs. The conductance is decreased when they are present within the constriction (see the blue and red lines in Fig. 2). The conductance maps for the

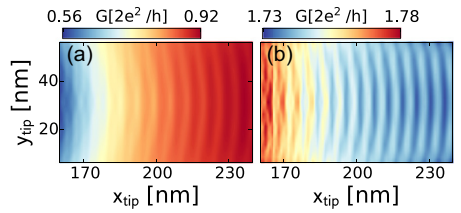

FIG. 7. The conductance maps as functions of the tip position for the etched QPCs without the singly connected atoms at the constriction. The area covered by the map is shown in Fig. 5(b) by the dashed rectangle. Open boundary conditions are applied. In (a) the Fermi energy is 0.312 eV, and in (b) it is 0.37 eV (b), i.e., the work points marked with the orange and light green points on the red conductance line in Fig. 2(a).

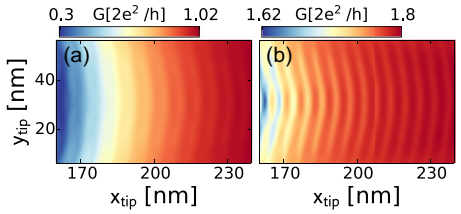

FIG. 8. Same as Fig. 7, but for the patched QPC. The Fermi energy is (a) 0.327 eV and (b) 0.37 eV; the work points are marked with the orange and light green points in Fig. 2(b).

etched QPC are given in Figs. 5(b) and 9. The map changes within the constriction, but the oscillation period that is due to the backscattering at a distance from the QPC, which this paper is about, remains unchanged.

E. Conductance maps with bulk scatterers off the constriction

We consider the influence of scattering by strong local perturbation due to the fluorine adatoms bound to the carbon lattice at a distance from the constriction. Two adatoms are considered with the positions marked by dots in Fig. 10. We model scanning gate microscopy of fluorinated graphene with $V_t = 0.5$ eV. In the conductance map we observe elliptical features near the adatoms superimposed on the conductance oscillation pattern with the period of half the Fermi wavelength characteristic of the clean sample. To improve the visibility of the signal, in Fig. 10(b) we plot a derivative of the conductance in Fig. 10(a). The ellipses plotted in Fig. 10 are drawn for the conditions of the interference of the wave functions incident from the QPC and backscattered by the tip and impurity, as described in the following section.

IV. DISCUSSION

The current distribution for the etched QPC is displayed in Fig. 11 with the interference fringe pattern between the QPC and the tip that results from the tip-induced backscattering. The white circle in Fig. 11 indicates the position where the effective tip potential equals E_F, i.e., the $n-p$ junction. In Fig. 11(b) a zoom of the rectangle marked in Fig. 11(a) is displayed with the current orientation given by the vector map. Note that the current at the cross section of the computational box is not necessarily conserved, as it can flow to the upper and lower contacts. The current in the entire infinite system, however, is always conserved. The current is focused by the circular $n-p$ junction and disperses to the right of it in Fig. 11(b).

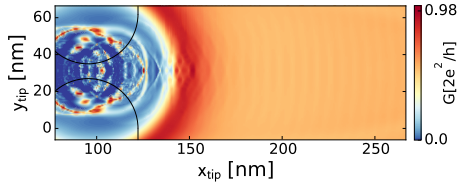

FIG. 9. The conductance as a function of the SGM tip position for nanoribbons with etched QPCs for a Fermi energy of 0.312 eV with singly connected atoms, with open boundary conditions and a vertical probe.

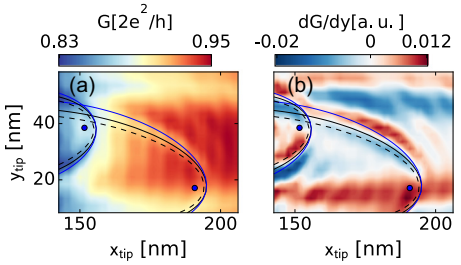

FIG. 10. The conductance as a function of the SGM tip position for nanoribbons with etched QPCs for a Fermi energy of 0.37 eV (a) with fluorine adatoms and (b) derived with respect to the vertical axis of (a) to enhance the visibility of the ellipselike fringes. Fluorine adatom positions are marked by blue circles.

In the Klein tunneling effect the Fermi electron incident on a perpendicular barrier larger than E_F is perfectly transmitted for the normal incidence angle, and the transmission probability is less than 1 for other incidence angles [21,22]. For a non-normal incidence, the current is partially reflected and partially transmitted and refracted by the $n-p-n$ junction [45,46]. In Fig. 11 a normal current along the axis of the system indeed passes across the junction. The tip potential deflects the currents inside the central p conductivity region, and only the precisely normal component of the current passes through undeflected. Other incidence angles contribute to backscattering.

The angular dependence of the scattering by a circular potential in graphene has been described for an incident plane wave in Ref. [46]. In our case the wave function coming from the QPC opening is not a plane wave; it is closer to a circular wave, which contributes to a deviation of the incidence angles from normal. Moreover, a tip potential that has an electrostatic origin is bound to possess a smooth profile. According to Ref. [23], for a smooth potential profile the transmission probability drops steeply below 100% already at a low deviation of the incidence angle from normal.

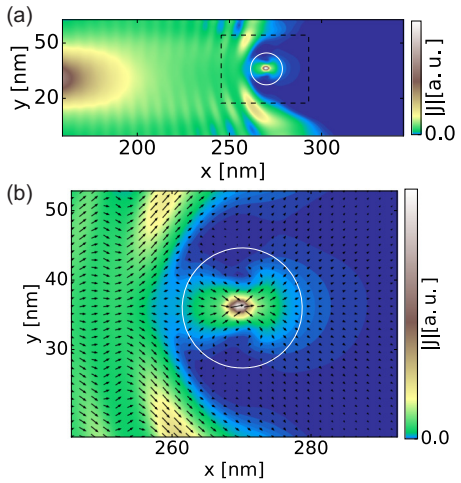

FIG. 11. (a) The current distribution for the etched QPC with the tip located at the axis of the system for $E_F = 0.312$ eV. The QPC center is set at $x = 100$ nm. The color map shows the length of the current vector. The white circle shows the $n-p$ junction for $V_t = 1.25$ eV. (b) Zoom of the dashed rectangle in (a) with the current orientation displayed by vectors.

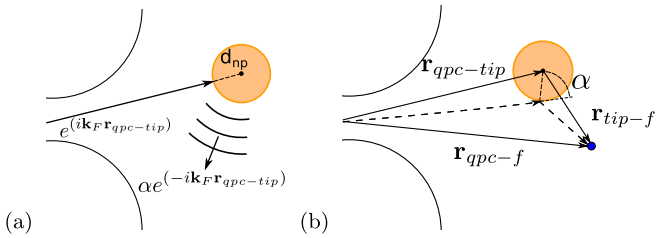

FIG. 12. (a) Scheme of the scattering by the tip-induced $n-p$ junction. (b) Scheme of the scattering between the tip and fluorine atom.

Let us consider a simple model for conductance oscillations far from the QPC. The QPC is a source of a circular wave function, and the SGM tip induces backscattering as argued above and shown in Fig. 12(a). The wave function incident from the QPC is partially reflected back to the opening [Fig. 12(a)]. The incident wave $\Psi_{in}(\mathbf{r}_{\rm tip}) = \exp[i\mathbf{k}_F(\mathbf{r}_{qpc} - \mathbf{r}_{\rm tip})]$ and the wave backscattered by the tip $\Psi_{sc}(\mathbf{r}_{\rm tip}) = \exp[-i\mathbf{k}_F(\mathbf{r}_{qpc} - \mathbf{r}_{\rm tip})]$ superpose and create a standing wave between the tip and the QPC. The electron density modulation can be described by

$$\left|\Psi(\mathbf{r}_{\rm tip})\right|^2 \propto \cos[2\mathbf{k}_F(\mathbf{r}_{\rm tip} - \mathbf{r}_{qpc})]. \tag{5}$$

This form of the scattering density gives rise to a conduction map that oscillates with the tip position, with a period of $\lambda_F/2$, where $\lambda_F = \frac{2\pi}{|\mathbf{k}_F|}$. The Fermi vector can be calculated for low energy from the graphene linear dispersion relation [36]:

$$k_F = \frac{2}{3}\frac{E_F}{t a_{CC}}. \tag{6}$$

In Fig. 13 the cross sections along the axis of the system of Figs. 6(a) and 6(b) are shown together with a cosine shifted in phase and offset to adjust to the conductance calculated from the quantum scattering problem. Far from the QPC, the modeled conductance is close to a cosine with a k_F that agrees with the wave vector obtained from the dispersion

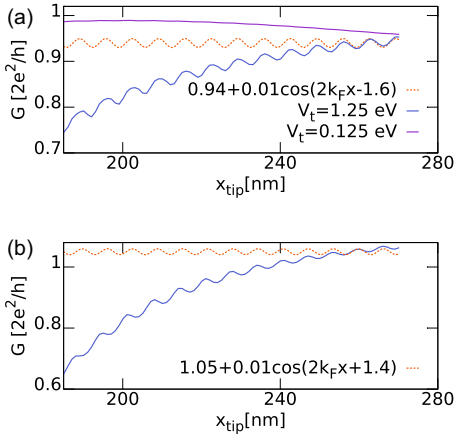

FIG. 13. The blue lines show the cross sections of the conductance maps along the symmetry axis of the device. (a) corresponds to Fig. 6(a) for an etched QPC with $E_F = 0.312$ eV, and (b) corresponds to Fig. 6(b) for a patched QPC with $E_F = 0.327$ eV. The dashed lines indicate the cosine with k_F. From Eq. (6) we find $k_F = 0.4695$ nm^{-1} for $E_F = 0.312$ eV in (a) and $k_F = 0.493$ nm^{-1} for $E_F = 0.327$ eV in (b).

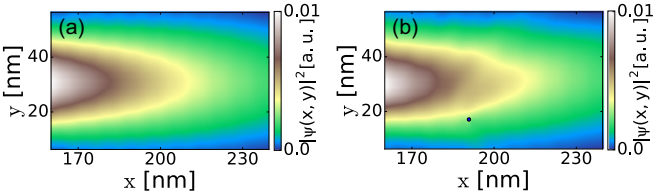

FIG. 14. The local density of states for $E_F = 0.312$ eV in the absence of the tip for the etched constriction (a) in pure graphene and (b) with fluorine adatoms.

relation of graphene. As seen in Figs. 5(b) and 6–9, far from the QPC the oscillations can be described by this simple model. In Fig. 13 with the purple line we mark the results obtained for $V_t = 0.125$ eV, which is below E_F. In this case no backscattered interference pattern is observed. We find that formation of the $n-p$ junction by the tip is a necessary condition for observation of the interference fringes.

The signal observed in the presence of scattering near the fluorine adatoms with the elliptical features in the conductance map in Fig. 10 is similar to the one identified recently in III-V semiconductors [43] as being due to the interference signal induced by scattering by the tip and a fixed defect. The interference paths are schematically shown in Fig. 12(b). Figure 12(a) illustrates backscattering by the $n-p$ junction induced by the tip resulting in the interference pattern with half the flux quantum discussed above. In Fig. 12(b) the electron wave incident from the QPC to the fluorine adatom interferes with the wave that is scattered by the tip-induced $n-p$ junction. The resulting conductance pattern can be approximately described by

$$G \propto \cos\left[k_F(r_{qpc-tip-f} - r_{qpc-f})\right]. \tag{7}$$

In Fig. 10 with the dashed lines we plot the isolines of $r_{qpc-tip-f} - r_{qpc-f} = \lambda_F/2$. The dashed ellipse corresponds to a pointlike tip, while the solid black line in Fig. 10 accounts for the finite radius of the $n-p$ junction $d_{np} = d\sqrt{\frac{V_t}{E_F} - 1}$. The black solid line in Fig. 10 was obtained for the condition $r_{qpc-tip-f} - r_{qpc-f} - d_{np} = \lambda_F/2$. A still closer approximation is obtained when one accounts for the dependence of the penetration depth [43] of the electron incidence angle α [see Fig. 12(b)]. For the blue solid line in Fig. 10 we considered the condition $r_{qpc-\mathrm{tip}-f} - r_{qpc-f} - d\sqrt{\frac{V_t}{E_F\cos(\alpha)} - 1} = \lambda_F/2$. In conclusion, in the presence of the defects the conductance map resolves the interference involving the tip, the QPC, and the defect, similar to what was previously described for III-V semiconductors.

The incomplete transmission in the Klein effect for electron incidence deviating from normal was used for construction of the $n-p-n$ Fabry-Pérot interferometers [47,48] in graphene. At $n-p-n$ junctions [49–52] interference of refracted waves in ballistic graphene appears in the scattering electron density, which is referred to as the local density of states [49]. The present work deals with SGM with spatial resolution of the standing waves in conductance maps and not only in the local density of states. The present idea does not require sharp $n-p$ junctions or a pointlike injection and detection of the current as in the Veselago lensing [49–52]. Figure 14 shows the probability density without the SGM tip for the electrons coming from the left terminal for pristine graphene [Fig. 14(a)] and with fluorine adatoms [Fig. 14(b)]. For dilute fluorinated graphene the backscattering by the fluorine adatom is resolved in the density plot in Fig. 14(b). There is no correlation between the densities and the conductance maps. The SGM maps resolve the quantum transport properties or in-plane conductance of the sample when the tip becomes the source of additional scattering. In contrast to the 2DEG in III-V quantum wells the surface electron gas in graphene can be alternatively studied with scanning tunneling microscopy (STM) [49–51]. In this configuration the tunneling microscope acts as a contact and not as a gate electrode. Instead of the scattering effects involving the tip STM resolves the local density of states.

Ref. [4] provided a SGM map of a graphene QPC for nominal tip potential set at $V_t = -0.5$ eV. The resistance map of this work [4] resolved only the QPC itself and not the interference fringes that were described here. The nominal V_t value given in Ref. [4] is an unscreened parameter, and it is not granted that the screened tip potential was strong enough to induce formation of the $n-p$ junction since no control of E_F was demonstrated [4]. Nevertheless, the present work indicates that observation of the spatial maps of the backscattering interference pattern in graphene is not excluded by the Klein tunneling effect.

V. SUMMARY AND CONCLUSIONS

We have studied current constriction by graphene QPCs formed by a gap between two biased bilayer patches and by a narrowing of a graphene ribbon using an atomistic tight-binding method and a Landauer approach. We considered conductance mapping as a function of a floating probe position. For this purpose open boundary conditions on the output side of the QPC were introduced in order to produce an image clean from backscattering by the edges and consequences of multiple Fermi wavelengths resulting from subband quantization. With the open boundary conditions simulating an infinite graphene plane on the output side of the QPC we found a clear interference pattern in the conductance map with a period of half the Fermi wavelength characteristic of the backscattering by the tip. The interference is observed only if the tip induces an $n-p$ junction in graphene. The backscattering of the electron wave function that occurs because of the circular-tip-induced $n-p$ junction for electron incidence at angles that deviate from normal is enough for the interference to be observed in the calculated conductance images. The finding that the Klein effect does not prevent observation of standing waves induced by the tip in graphene opens perspectives for experimental determination of the current distribution, current branching by scattering defects, coherence length, etc.

ACKNOWLEDGMENTS

This work was supported by the National Science Centre (NCN) according to decision DEC-2015/17/B/ST3/01161, by PL-Grid infrastructure and by Ministry of Science and Higher Education within the AGH University of Science and Technology statutory activity task no. 11.11.220.01.

[1] C. Beenakker and H. van Houten, Solid State Phys. **44**, 1 (1991).
[2] B. J. van Wees, H. van Houten, C. W. J. Beenakker, J. G. Williamson, L. P. Kouwenhoven, D. van der Marel, and C. T. Foxon, Phys. Rev. Lett. **60**, 848 (1988).
[3] H. Sellier, B. Hackens, M. G. Pala, F. Martins, S. Baltazar, X. Wallart, L. Desplanque, V. Bayot, and S. Huant, Semicond. Sci. Technol. **26**, 064008 (2011).
[4] S. Neubeck, L. Ponomarenko, A. Mayorov, S. Morozov, R. Yang, and K. Novoselov, Phys. E (Amsterdam, Neth.) **44**, 1002 (2012).
[5] M. R. Connolly, K. L. Chiu, A. Lombardo, A. Fasoli, A. C. Ferrari, D. Anderson, G. A. C. Jones, and C. G. Smith, Phys. Rev. B **83**, 115441 (2011).
[6] N. Pascher, D. Bischoff, T. Ihn, and K. Ensslin, Appl. Phys. Lett. **101**, 063101 (2012).
[7] A. G. F. Garcia, M. König, D. Goldhaber-Gordon, and K. Todd, Phys. Rev. B **87**, 085446 (2013).
[8] M. R. Connolly, R. K. Puddy, D. Logoteta, P. Marconcini, M. Roy, J. P. Griffiths, G. A. C. Jones, P. A. Maksym, M. Macucci, and C. G. Smith, Nano Lett. **12**, 5448 (2012).
[9] R. K. Rajkumar, A. Asenjo, V. Panchal, A. Manzin, Ã. Iglesias-Freire, and O. Kazakova, J. Appl. Phys. **115**, 172606 (2014).
[10] C. Chua, M. Connolly, A. Lartsev, T. Yager, S. Lara-Avila, S. Kubatkin, S. Kopylov, V. Fal'ko, R. Yakimova, R. Pearce, T. J. B. M. Janssen, A. Tzalenchuk, and C. G. Smith, Nano Lett. **14**, 3369 (2014).
[11] S. Morikawa, Z. Dou, S.-W. Wang, C. G. Smith, K. Watanabe, T. Taniguchi, S. Masubuchi, T. Machida, and M. R. Connolly, Appl. Phys. Lett. **107**, 243102 (2015).
[12] S. Bhandari, G.-H. Lee, A. Klales, K. Watanabe, T. Taniguchi, E. Heller, P. Kim, and R. M. Westervelt, Nano Lett. **16**, 1690 (2016).
[13] M. D. Petrović, S. Milovanović, and F. Peeters, Nanotechnology **28**, 185202 (2017).
[14] K. Kolasiński, A. Mreńca-Kolasińska, and B. Szafran, Phys. Rev. B **95**, 045304 (2017).
[15] M. A. Topinka, B. J. LeRoy, R. M. Westervelt, S. E. J. Shaw, R. Fleischmann, E. J. Heller, K. D. Maranowski, and A. C. Gossard, Nature (London) **410**, 183 (2001).
[16] B. J. LeRoy, A. C. Bleszynski, K. E. Aidala, R. M. Westervelt, A. Kalben, E. J. Heller, S. E. J. Shaw, K. D. Maranowski, and A. C. Gossard, Phys. Rev. Lett. **94**, 126801 (2005).
[17] M. P. Jura, M. A. Topinka, M. Grobis, L. N. Pfeiffer, K. W. West, and D. Goldhaber-Gordon, Phys. Rev. B **80**, 041303 (2009).
[18] N. Paradiso, S. Heun, S. Roddaro, L. Pfeiffer, K. West, L. Sorba, G. Biasiol, and F. Beltram, Phys. E (Amsterdam, Neth.) **42**, 1038 (2010).
[19] B. Brun, F. Martins, S. Faniel, B. Hackens, G. Bachelier, A. Cavanna, C. Ulysse, A. Ouerghi, U. Gennser, D. Mailly, S. Huant, V. Bayot, M. Sanquer, and H. Sellier, Nat. Commun. **5**, 4290 (2014).
[20] C. Gutiérrez, L. Brown, C.-J. Kim, J. Park, and A. N. Pasupathy, Nat. Phys. **12**, 1069 (2016).
[21] M. I. Katsnelson, K. S. Novoselov, and A. K. Geim, Nat. Phys. **2**, 620 (2006).
[22] P. E. Allain and J. N. Fuchs, Eur. Phys. J. B **83**, 301 (2011).
[23] J. Cayssol, B. Huard, and D. Goldhaber-Gordon, Phys. Rev. B **79**, 075428 (2009).
[24] C. Schulz, R. L. Heinisch, and H. Fehske, Quantum Matter **4**, 346 (2015).
[25] R. Yang, L. Huang, Y.-C. Lai, and C. Grebogi, Phys. Rev. B **84**, 035426 (2011).
[26] Y.-M. Lin, V. Perebeinos, Z. Chen, and P. Avouris, Phys. Rev. B **78**, 161409 (2008).
[27] N. Tombros, A. Veligura, J. Junesch, M. H. D. Guimaraes, I. J. Vera-Marun, H. T. Jonkman, and B. J. van Wees, Nat. Phys. **7**, 697 (2011).
[28] B. Terrés, L. A. Chizhova, F. Libisch, J. Peiro, D. Jörger, S. Engels, A. Girschik, K. Watanabe, T. Taniguchi, S. V. Rotkin, J. Burgdörfer, and C. Stampfer, Nat. Commun. **7**, 11528 (2016).
[29] A. Kinikar, T. P. Sai, S. Bhattacharyya, A. Agarwala, T. Biswas, S. Sarker, H. R. Krishnamurthy, M. Jain, V. Shenoy, and A. Ghosh, Nat. Nanotechnol. **12**, 564 (2017).
[30] F. Muñoz-Rojas, D. Jacob, J. Fernández-Rossier, and J. J. Palacios, Phys. Rev. B **74**, 195417 (2006).
[31] S. Ihnatsenka and G. Kirczenow, Phys. Rev. B **85**, 121407 (2012).
[32] S. Ihnatsenka and G. Kirczenow, Phys. Rev. B **86**, 075448 (2012).
[33] E. McCann and M. Koshino, Rep. Prog. Phys. **76**, 056503 (2013).
[34] E. McCann, Phys. Rev. B **74**, 161403 (2006).
[35] E. V. Castro, K. S. Novoselov, S. V. Morozov, N. M. R. Peres, J. M. B. Lopes dos Santos, J. Nilsson, F. Guinea, A. K. Geim, and A. H. Castro Neto, Phys. Rev. Lett. **99**, 216802 (2007).
[36] A. H. Castro Neto, F. Guinea, N. M. R. Peres, K. S. Novoselov, and A. K. Geim, Rev. Mod. Phys. **81**, 109 (2009).
[37] F. Xia, D. B. Farmer, Y.-M. Lin, and P. Avouris, Nano Lett. **10**, 715 (2010).
[38] J. Park, S. B. Jo, Y.-J. Yu, Y. Kim, J. W. Yang, W. H. Lee, H. H. Kim, B. H. Hong, P. Kim, K. Cho, and K. S. Kim, Adv. Mater. **24**, 407 (2012).
[39] K. He, A. W. Robertson, S. Lee, E. Yoon, G.-D. Lee, and J. H. Warner, ACS Nano **8**, 12272 (2014).
[40] S. Irmer, T. Frank, S. Putz, M. Gmitra, D. Kochan, and J. Fabian, Phys. Rev. B **91**, 115141 (2015).
[41] B. Partoens and F. M. Peeters, Phys. Rev. B **74**, 075404 (2006).
[42] K. Kolasiński and B. Szafran, Phys. Rev. B **88**, 165306 (2013).
[43] K. Kolasiński, B. Szafran, B. Brun, and H. Sellier, Phys. Rev. B **94**, 075301 (2016).
[44] D. J. Klein and L. Bytautas, J. Phys. Chem. A **103**, 5196 (1999).
[45] G.-H. Lee, G.-H. Park, and H.-J. Lee, Nat. Phys. **11**, 925 (2015).
[46] J. Cserti, A. Pályi, and C. Péterfalvi, Phys. Rev. Lett. **99**, 246801 (2007).
[47] A. V. Shytov, M. S. Rudner, and L. S. Levitov, Phys. Rev. Lett. **101**, 156804 (2008).
[48] A. Young and P. Kim, Nat. Phys. **5**, 222 (2009).
[49] V. Cheianov, V. Fal'ko, and B. Altshuler, Science **315**, 1252 (2007).
[50] Y. Xing, J. Wang, and Q.-f. Sun, Phys. Rev. B **81**, 165425 (2010).
[51] A. G. Moghaddam and M. Zareyan, Phys. Rev. Lett. **105**, 146803 (2010).
[52] F. Libisch, T. Hisch, R. Glattauer, L. Chizova, and J. Burgdörfer, J. Phys. Condens. Matter **29**, 114002 (2017).